Investigating the Viability of Material Extrusion Additive Manufacturing of Inconel 718 for Fatigue Driven Applications

Matthew Mathesius[1], Erica Kozak[1], Onome Scott-Emuakpor, Ph.D.[2], and Sanna F. Siddiqui, Ph.D.[3*]
[1,3]Florida Polytechnic University, Lakeland, FL, 33805,USA
[2]Hyphen Innovations LLC, Dayton, Ohio, 45431,USA

Inconel 718 (IN718) is a nickel-based superalloy commonly used in aerospace applications due to its exceptional performance in high-temperature environments. The use of metal additive manufacturing (AM) technologies (i.e., laser powder bed fusion (LPBF), binder jetting (BJ), and direct energy deposition (DED)) to produce these components have become more prevalent given their exhibited comparable mechanical performance to wrought counterparts. Nevertheless, the considerable expense in acquisition and maintenance of these AM technologies limits their potential to provide a cost-efficient approach from part design to implementation. This study focuses on assessing the viability of the low-cost material extrusion additive manufacturing (MEAM) technology, on manufacturing Inconel 718 samples for fatigue applications. The MEAM process which is dictated by its manufacturing of a component from metal powder bounded within a polymeric filament through the extrusion process, is used to print varying IN718 specimen geometries (i.e., cube, tensile, torsion, and rotating bending fatigue test specimens) in the as-built (green) state. The role of processing parameters (i.e., increased flow rate, hot end temperature etc.) on part quality and defect presence was assessed, and monotonic tensile and torsion tests were performed to assess the structural integrity and mechanical properties of MEAM IN718 in the as-built (green state). This study is novel in that it sets the framework for optimization of 3D print processing parameters on as-built (green) fatigue specimen design prior to future work, which will assess impacts of the debinding and sintering process.

I. Introduction

Inconel 718 (IN718) is a nickel-based superalloy largely used in aerospace components such as gas engine turbine blades and discs due to its favorable strength and fatigue life in high temperature environments upwards of 650°C [1], alongside its resistance to wear, creep, and corrosion [2]. Despite these desirable properties, due to the complex geometries of aircraft components, difficulty in machining, and intense wear the IN718 causes on subtractive equipment [2], additive manufacturing (AM) has become a researched alternative to traditional subtractive manufacturing methods. AM also provides the additional benefits of increased flexibility in design and allowance for rapid prototyping of components. Metal AM processes can be classified into the following technologies: Binder Jetting Printing (BJP), Laser Powder Bed Fusion (L-PBF), Direct Energy Deposition (DED), and Material Extrusion (MEAM). An assessment of the Metal AM market has shown that the L-PBF is the most used printing process in industry at this stage, despite being reported as having a greater setup and production cost compared to MEAM [3]. This cost differential is a function of the equipment required, alongside the safety preventative measures necessary when working with laser power and metal powders that exhibit safety hazards ranging from carcinogenic to flammability in nature. These include, but are not limited to, installation of ventilation systems, due to direct

---

[1] Undergraduate Research Assistant, Department of Mechanical Engineering

[2] Chief Executive Officer (CEO)/Founder, Hyphen Innovations LLC

[3*] Assistant Professor, Department of Mechanical Engineering, Young Professional AIAA Member, Corresponding Author (E-mail: ssiddiqui@floridapoly.edu)

exposure and handling of metal powders [3]. Differentiating these varying technologies, L-PBF processes, such as Selective Laser Melting (SLM), uses a focused laser to heat metallic powder laid onto a print bed one layer at a time. A rolling mechanism adds the metallic powder for the following layer, repeating the layer deposition process of the part until the component is complete. BJP follows a similar technique but is differentiated using liquid binder that is used to solidify the metallic powder when a UV lamp or other minor heating source is present. This heat source is notably different from L-PBF and DED, in which both of those processes require a more expensive, power heat source. BJP is also seen as favorable due to the lack of support structure requirements that are seen in other AM methods. However, its notably low yield in the metal AM market is largely attributed to high porosity, as research has shown the relative density is typically 50-60% for BJP parts when compared to expected theoretical part density [4]. DED, on the other hand, is differentiated from L-PBF by how the material is deposited. Unlike the roller mechanisms seen in L-PBF, setups often see utilization of both an energy source and either a powder feeder or wire arc that meet to melt the material onto the substrate. Both movement of the substrate and energy source is seen, which will form layer-by-layer until print completion [5,6].

While these metal AM technologies have been widely adopted, presence of microstructural defects, developed through the manufacturing process limits their use for fatigue-driven applications. In the case of L-PBF, one of the key defects is lack of fusion (LOF) defects [7,8]. LOF causes the melt pool of each layer to not properly overlap and fuse together. These non-spherical pores act as crack nucleation sites and are thus determinantal for fatigue life [9,10]. Porosity presence can result from gas atomization when creating metallic powder and overall poor powder quality [11]. Sources of microstructural defects can arise from variation in 3D print parameters such as laser power, scanning speed. Optimization of these print parameters in addition to use of post-processing techniques such as hot isostatic pressing (HIP) has been shown to minimize the presence of porosity in printed parts [9,12].

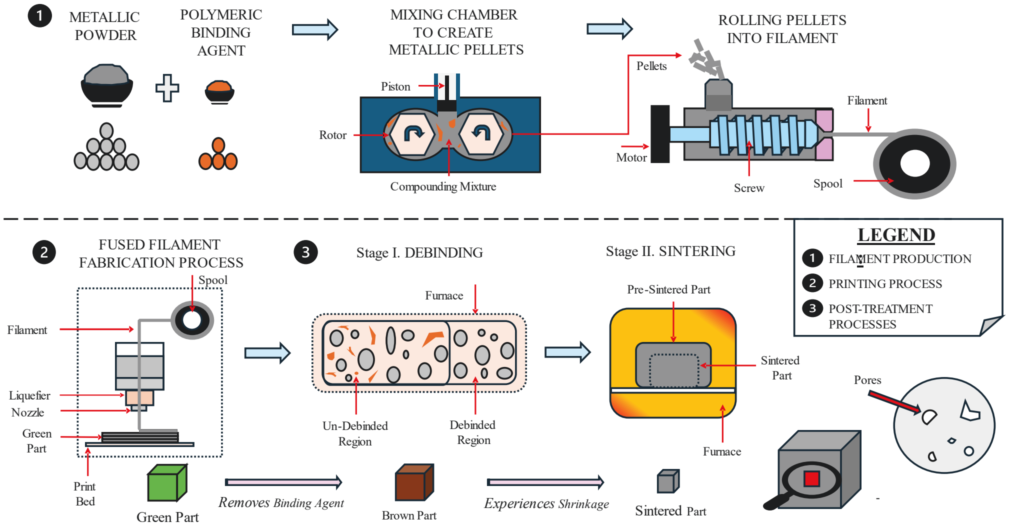

Fig. 1: Material Extrusion Additive Manufacturing (MEAM) Process

Considerable literature has been reported on LPBF Inconel 718, with only more recent work evaluating the role of MEAM on mechanical performance of Inconel 718. Through the MEAM process shown in Fig 1, metallic pellets are created from metallic powder and a polymeric binding. This binding agent is comprised of three components: a non-viscous primary binder of low molecular weight (50-90% of composition), a thermoplastic backbone that holds shape after the debinding process (<50% of composition), and additional additives to ensure metallic particles disperse uniformly throughout the material [13]. These metallic pellets are then spun into thin strands of filament that are extruded through a nozzle at heated temperatures during printing. The layer-by-layer printed component made through this process is known as a *green part.* Print parameters affecting the performance of the part typically include infill, print speed, rate of heating, and layer thickness [14,15].

In the first of two post-processing treatments, debinding, the primary objective is to eliminate the presence of the primary binder within the material. Heat debinding is done by applying controlled temperatures to the part in a programmable furnace for set time intervals. Sintering is then conducted at higher temperatures (1200-1300C for IN718 [16–19]) to fuse the metallic particles within the component together, resulting in increases in mechanical properties such as strength, ductility, and corrosion resistance [15]. Furthermore, sintering results in enhancements of percent density which correlates to lower porosity in the component.

As evident in Fig 1, one of the major defects exhibited in MEAM is shrinkage during the sintering process. Estimates show shrinkage of varying extruded materials is estimated to fall within approximately 20% or less of original print dimensions, [20,21]. Consideration in the sizing of green parts is thus critical when designing components to be made under MEAM. Secondarily, surface roughness of printed components becomes a critical issue when examining mechanical and fatigue performance. Increased surface roughness results in higher magnitudes of stress concentrations at the exterior, becoming most critical under flexural and torsional loading conditions, where the stress distribution is maximum at the surface. Finally, considerations into reduction of porosity developed due to loss of polymer binder material during the MEAM process is critical to ensure mitigation of stress concentration sites that serve as precursors to fatigue failure. In terms of mechanical performance, Table 1 showcases the variation between these metal AM manufacturing methods in yielding enhanced mechanical properties for IN718. In Table 1, σ_{YS} is the yield strength, σ_{UTS} is the ultimate tensile strength, and EL% is the elongation. DED and L-PBF parts show close to comparable tensile properties, with MEAM studies being much more limited.

Table 1: Tensile properties reported for IN718 manufactured through varying metal AM processes

Method	Condition	σ_{YS} (MPa)	σ_{UTS} (MPa)	EL (%)	Reference
L-PBF	As-built, horizontal build orientation	680.18 ± 12	970.25 ± 11.25	31.62 ± 0.3	[10]
L-PBF	As-built, horizontal build orientation	643 ± 63	991 ± 62	13 ± 6	[22]
L-PBF	As-built, vertical build orientation	572 ± 44	904 ± 22	19 ± 4	[22]
DED	As-deposited, vertical build orientation	590	845	11	[23, 32]

Fatigue testing of MEAM IN718, however, is not as heavily a researched field compared to L-PBF. An assessment of axial fatigue studies of Inconel 718 has shown that the L-PBF specimens exhibited longer fatigue life at lower strain amplitudes compared to wrought IN718, but not at higher strain amplitudes [24]. It was also determined that HIP negatively impacted the low-cycle fatigue life of tested L-PBF specimens [24]. A DED study further showed comparable results to wrought IN718, with slightly lower fatigue life performance at both room and elevated temperatures [25]. This study further saw comparable fatigue resistance to wrought IN718 at elevated temperatures of 650°C [25]. Reviewing bending fatigue studies on L-PBF IN718, however, one fully reversed test showed that non-heat treated, horizontally built IN718 specimens experienced longer fatigue lives and moderate fatigue damage relative to vertical and angled counterparts [26]. A second study showed that wrought and L-PBF IN718 experienced lower fatigue behavior under rotary bending fatigue testing at room temperature and similar fatigue behavior at elevated temperatures [27].

This study will begin the process of examining the possibility of using MEAM parts over the more expensive metal AM manufacturing methods, through specimen manufacturing for axial, torsional and rotating-bending fatigue applications. Monotonic tensile and torsional properties of as-built MEAM Inconel 718 (green part) composites, and failure under these varying mechanical loading conditions will be presented. The importance of specimen design and optimized print parameters will be presented by analyzing part quality and the microstructural defects present in MEAM IN718 prior to the debinding and sintering stage (green parts). Analysis of the efficacy of the selected design and parameters will be elaborated on alongside with recommendations for the debinding and sintering processes.

II. Experimental Design

To assess the part quality of MEAM as-built IN718 samples for fatigue driven applications, varying different specimen geometries were manufactured using an Original Prusa i3 MK3S+ 3D printer with Virtual Foundry's 1.75mm filament comprised of a mixture of a PLA-like polymeric binding and IN718 metallic powder extruded through a 0.6mm E3D V6 nozzle. The nozzle size of 0.6mm was the size of E3D V6 nozzle recommended by Virtual Foundry [30].Virtual Foundry's FilaWarmer was attached between the spool and the extruder to transform the filament from a brittle state to a more flexible and pliable state prior to entering the extruder, with a schematic of the filament travel process shown in Fig 2a. The designed and 3D printed spool and FilaWarmer mounts were arranged colinear as seen in Fig. 2b, which guided the filament prior to entering the extruder. Before loading into the Original Prusa i3 MK3S+ 3D printer, the filament is inserted into the FilaWarmer and left in between the heating coils for approximately 30 seconds. The filament is then slightly fed through further, again stopping for 30 seconds before continuing to feed through the FilaWarmer. Through this iterative process, the initial filament to be loaded will spend approximately 1.5-2 minutes within the FilaWarmer prior to exiting to ensure the filament is flexible enough to not break inside of the extruder [30]. Once the filament passes through the extruder, the layer-by-layer deposition of the heated filament creates the desired final part geometry, as seen in Fig 2c.

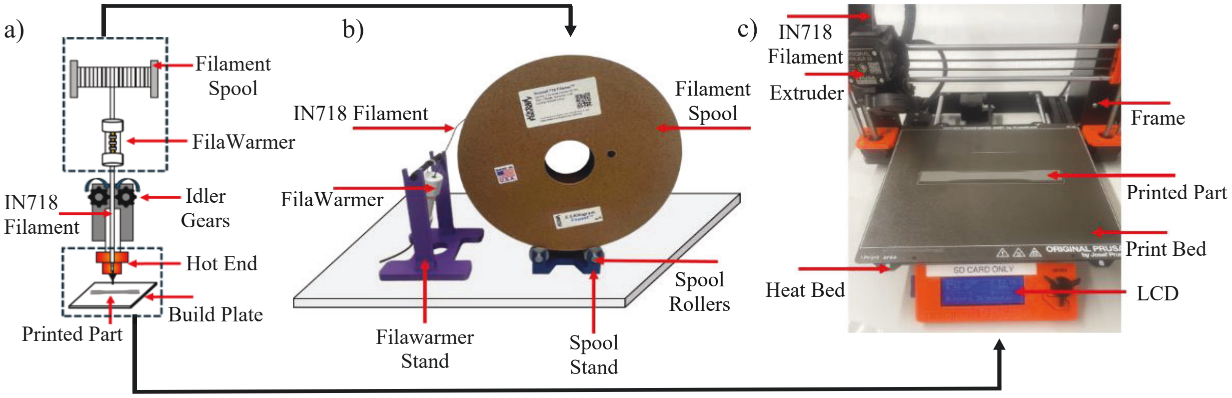

Fig. 2: a) Schematic of filament travel process through the FilaWarmer, idler gears, hot end, and nozzle before extruding onto the print bed, b) Schematic of experimental setup of filament guidance through the FilaWarmer prior to entering the extruder, and c) Original Prusa i3 MK3S+ 3D Printer used to manufacture the samples

The 3D print parameters used to manufacture MEAM IN718 samples (i.e., cube, tensile, torsion and rotating-bending fatigue specimens) were primarily set to the default parameters for Prusa PLA within the Prusa Slicer [28]. Specimens were manufactured along the X-build orientation with a print bed temperature of 60°C. Variations from these default parameters used to manufacture the test specimens printed in this study are depicted in Table 2. Based on varying iterations of print parameters, the higher hot-end temperature of 220°C resulted in superior bed adhesion and minimal filament solidification inside of the hot end. Additionally, various extrusion widths were increased to increase the density of different layer types [29], resulting in more solid parts.

Table 2: 3D print parameters used in manufacturing of all test specimens (i.e., cubes, tensile, torsion, and rotating-bending specimens) [28-30]

Parameter Name	Prusa Slicer PLA Default Settings	Optimized Parameters
Percent Infill	15%	100%
Hot End Temperature (All Layers)	215°C First Layer, 210°C Remaining Layers	220°C All Layers
Nozzle Size	0.4mm	0.6mm
First Layer Width	0.42mm	0.65mm
Default Extrusion Width, Perimeter Width, Infill Width, Solid Infill Width	0.45mm	0.65mm
Top Solid Infill Width	0.40mm	0.60mm
Support Material Width	0.35mm	0.55mm
Infill/Perimeter Overlap	10%	15%

IN718 green cube specimens with 25.4mm length, width and height dimensions, as seen in Fig 3a, were manufactured through the MEAM process to determine the effects of flow rate alterations on part quality. To this effect, comparative analysis was performed between recommended PLA standard flow rate of 95% [28] versus an increased flow rate of 130%. Density analysis was completed on these cubes to determine the effects of porosity under each of the print parameter conditions through use of a Mettler Toledo™ Standard ME Precision Lab Balance for mass measurements, and a Mitutoyo™ AOS Absolute Digimatic Caliper for specimen geometry measurements. Additionally, IN718 green specimens designed for monotonic tensile and torsion testing were printed based upon the specimen geometries shown in Fig. 3b and Fig. 3c, with an increased flow rate of 130%. Tensile test specimens were designed based upon the ASTM D638-14 Standard Type 1 specimen design with a gage length of 50mm and a gage thickness and width of 3.2mm and 13mm respectively. Torsion test specimens were manufactured with a gage length of approximately 50mm and gage diameter of 5.33mm respectively. MEAM as-built IN718 rotating bending fatigue test specimens were manufactured along the X and Z-build orientations, based upon the specimen design shown in Fig 3d. Due to the presence of overhangs in the X-build orientation for the torsion and rotating bending specimen designs, support material was generated for these prints. Similarly, to increase print stability for the Z-build orientation of the rotating bending specimen, a brim layer was added.

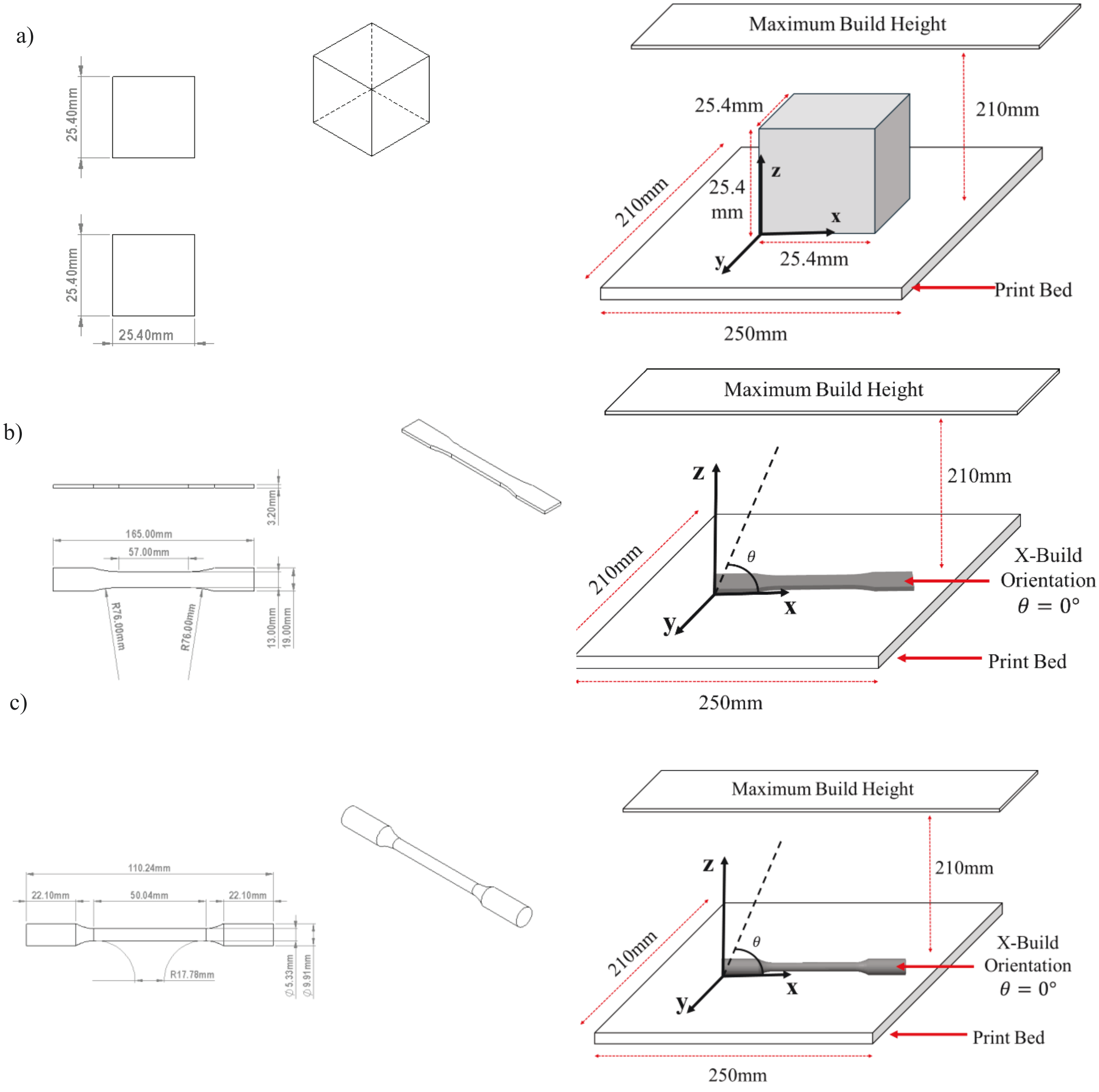

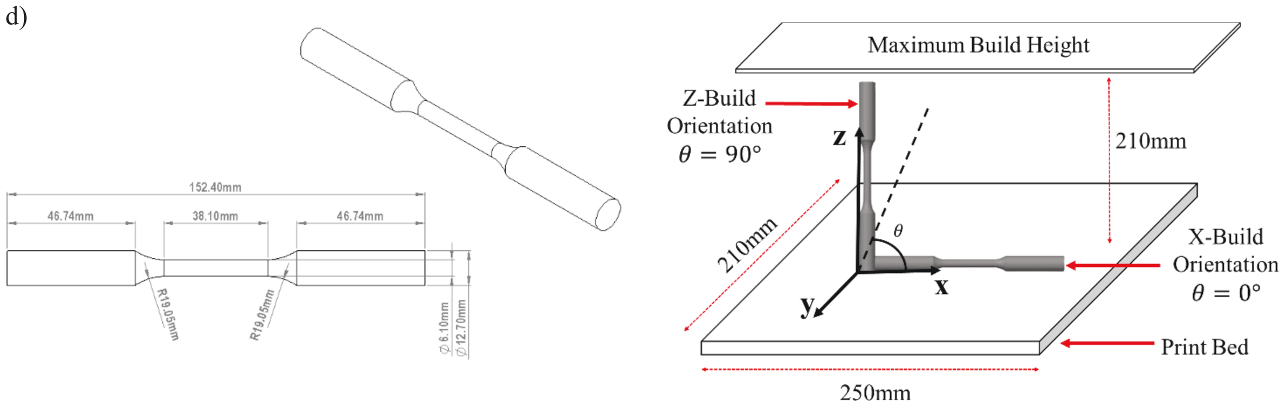

Fig. 3: Specimen geometry (left) and orientation on build platform (right): a) Cube specimen, b) Tensile test specimen, c) Torsion test specimen, and d) Rotating bending fatigue test specimen

For material testing and characterization, tensile specimens underwent monotonic tensile testing under displacement control at a displacement rate of 5.08mm/min using an Instron™ 5965 Universal Testing Machine with a 5kN load cell as shown in Fig 4a. Specimen failure was identified by complete fracture subject to tensile loading. For the tensile tests, the data output from the Instron™ 5965 Universal Testing Machine was received in applied load (Newtons) and extension of the gage section (mm). This was converted into a stress-strain curve assuming fully axial over a rectangular cross section defined by the gage width and thickness. Approximate strain was determined assuming the theoretical gage length of 50mm.

Similarly, torsion specimens underwent angle of twist control monotonic torsion testing at an angle of twist rate of 1.654 deg/s using the MTS Bionix™ Electromechanical Torsion Test Frame, as seen in Fig 4b. The data output from the MTS Bionix™ Electromechanical Torsion Test Frame was received in applied torque (N-m) and angle of twist (degrees). The applied torque was converted to shear stress assuming the gage section was a fully solid shaft and approximate shear strain was determined assuming the theoretical gage length of ~50mm. Specimen failure was identified by either complete fracture or significant drop in torque-carrying capacity of specimen subject to torsional loading.

Future work intends for the rotating bending specimen design to undergo fatigue testing on ADMET™ eXpert 9300 Series Rotating Bending Fatigue Tester, shown in Fig 4c, following successful manufacture of test specimens after the debinding and sintering process. Microstructural analysis of part quality and fracture response exhibited by green specimens was achieved using the Dino-Lite™ Edge Series Digital Microscope following multi-point calibration (Figure 4e), and Hitachi™ SU3500 Scanning Electron Microscope (SEM) in secondary electron mode at varying magnifications with energy levels ranging between 10-15kV and spot intensities between 40-50 (Figure 4d).

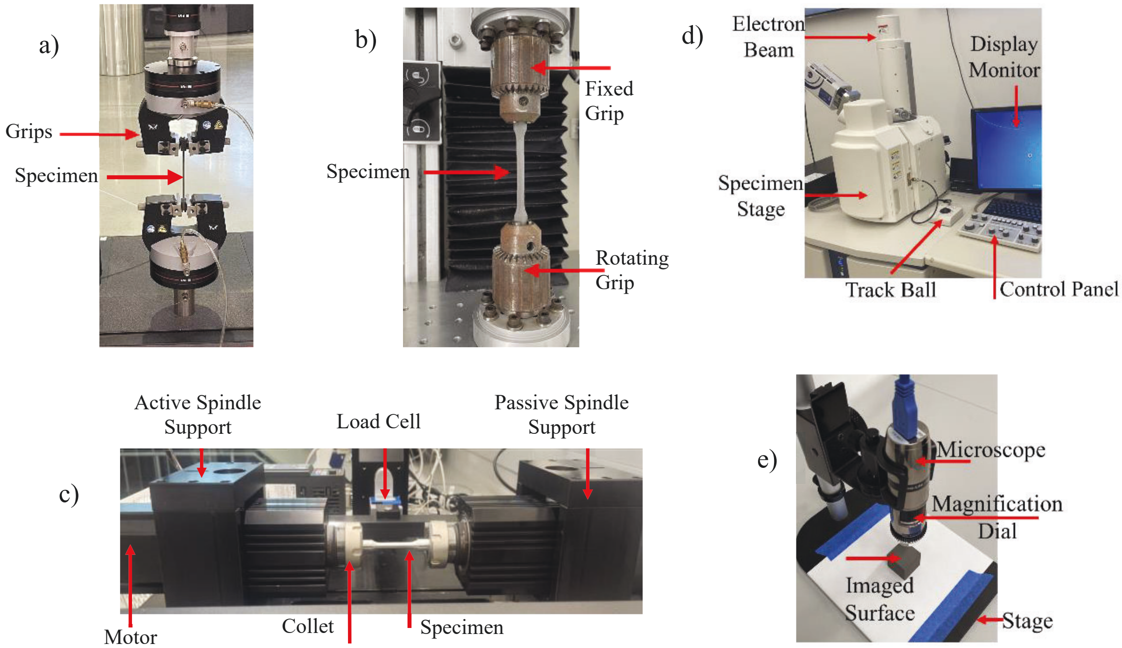

Fig. 4: a) Instron™ 5965 Universal Testing Machine, b) MTS Bionix™ Electromechanical Torsion Test Frame, c) ADMET™ eXpert 9300 Series Rotating Bending Fatigue Tester, d) DinoLite™ Edge Series Digital Microscope, and e) Hitachi™ SU3500 Scanning Electron Microscope

III. Results and Discussion

In this study, analysis is conducted on the presence of MEAM induced defects and the role of varying print parameter combinations on resulting part quality. Reporting on the qualitative effects (i.e., geometric tolerances achieved, microstructural analysis of porosity presence etc.) with varying print parameters is presented with failed and successful printed parts as a showcase of these findings. This study presents optimized print parameters for the manufacturing of cube, tensile, torsional and rotating-bending fatigue test specimens. The monotonic tensile and torsional performance and properties of these as-built (green) MEAM IN718 parts is reported to showcase the mechanical structural integrity of as-built MEAM components as a preface for fatigue testing in future work.

A. Cube Specimen Analysis

Geometric dimensionalization and mass measurements of the as-built green MEAM IN718 cube specimens manufactured using the optimized processing parameters in Table 2 with variation in flow rate are as presented in Table 3, compared with theoretically expected values. The theoretical mass of the cube is directly provided from the Prusa Slicer after inputting the filament density for MEAM IN718 filament (3.23g/cm^3). Each of the dimensions reported, and the mass the cubes were measured 3 times, with the average of those values reported herein. It is shown that both the average print volume, dimensions, and mass of the cubes manufactured, regardless of flow rate, were greater than the theoretically estimated values within the Prusa Slicer. Nevertheless, of the two cube samples manufactured with varying flow rate (95% versus 130%), the cube manufactured with an increased flow rate (i.e., 130%) resulted in a denser part relative to use of the standard flow rate of 95% and print value closer to theoretically expected part volume.

Table 3: Cube Specimen Density Analysis

Parameters	Dimensions [L x W x H] (cm)	Print Volume (cm^3)	Mass (g)	Estimated Density (g/cm^3)
Theoretical	2.5400 x 2.5400 x 2.5400	16.3870	53.0800	3.2391
Parameters	**Average Dimensions [L x W x H] (cm)**	**Average Print Volume (cm^3)**	**Average Mass (g)**	**Estimated Density (g/cm^3)**
Optimized Parameters, 95% Flow Rate	2.5527 x 2.5629 x 2.5400	16.6175	57.7771	3.4769
Optimized Parameters, 130% Flow Rate	2.5451 x 2.5502 x 2.5400	16.4859	58.8876	3.5720

Analyzing the numerical results, it is seen that the increased flow rate resulted in cubes with a higher mass and larger print volume. This is suggested to be attributed to the impact of overlapping layer lines [33], which becomes more likely as extrusion widths are increased as they were in the present study with the optimized set of print parameters used in manufacturing the specimens. Increasing the flow rate appeared favorable in printing specimens using MEAM IN718 filament. It appears that neither of the cube specimens exhibited any notable warping. Shrinkage was also not prevalent, as dimensions across the length, width, and height of the cubes remained relatively consistent. From an overall assessment of these MEAM induced defects, it appears that for maximizing part density, an increased flow rate of 130% appears to be effective. These findings agree with other sources on the presence of increased flow rate resulting in a greater material concentration, as a previous study reported that an increased flow rate resulted in enhanced mechanical properties for 3D printed PLA specimens due to the larger material density per unit area in which load is applied [31]. As these are preliminary results, future work will be performed to further confirm these findings.

B. Rotating Bending Fatigue Specimen Preparation

In an effort to assess the viability of the MEAM process in manufacturing specimens for fatigue testing (i.e., presence of minimal microstructural/surface defects), the role of processing parameters was assessed on manufacturing an X and Z-build rotating-bending fatigue test specimen. Figure 5a compares Z-build rotating-bending fatigue test specimens manufactured using optimized (Table 2) and unoptimized processing parameters (hot end temperature = 210°C and Prusa Slicer PLA default settings for extrusion width), with the flow rate maintained for both prints at 95%. As evident, the Z-build rotating-bending fatigue test specimen manufactured with lower hot end temperature and default Prusa Slicer PLA settings exhibited print failure. Further analysis of the failed Z-built specimen manufactured using unoptimized parameters, revealed considerable presence of porosity through microscopic imaging (Fig. 5c). In contrast to MEAM manufacturing of the cube, tensile, and torsion specimens, the increased flow rate from 95% to 130% resulted in failed prints for both the X and Z built specimens. Failure in the Z-build (not shown) was attributed to a nozzle jam, but more notably, the X-build specimen exhibited failure due to a layer line shift as seen in Fig 5b. Further experimentation and optimization to the current set of processing parameters provided in Table 2 will be necessary in limiting the presence of defects and ensuring successful as-built green parts for future rotating-bending fatigue testing.

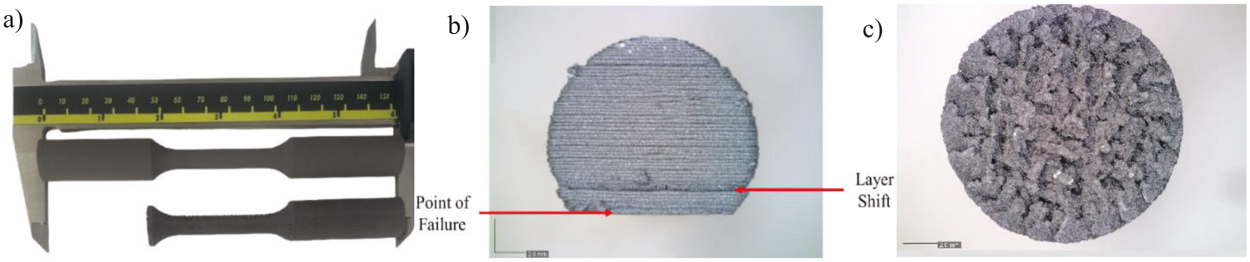

Fig. 5: a) Complete Z-build rotating bending fatigue specimen printed with optimized parameters (top) versus an incomplete, more porous Z-build rotating bending fatigue specimen with unoptimized parameters (bottom) at 95% flow rate, b) X-build rotating bending specimen that failed on a layer line that was in close proximity to the support material, c) Porosity evident in failed print of Z-build rotating bending fatigue specimen with unoptimized parameters

C. Tensile and Torsional Performance of As-built MEAM IN718

Tensile and torsional test specimens were manufactured using the optimized processing parameters presented in Table 2, and 130% increased flow rate. Prior to conducting monotonic tensile and torsion experiments on the as-built (green state) MEAM-produced samples, 3 measurements of the gage section of each sample were taken and averaged, as reported in Table 4. Also listed in Table 4 are the expected theoretical dimensions expected for each test specimen type. The theoretical mass is determined from the calculation from Prusa Slicer after inputting the IN718 filament density of 3.23 g/cm^3 and importing the respective specimen geometry. As the specimens were manufactured along the X-build orientation, the larger measured mass and gage diameters for the torsion specimens may be attributed to the surface roughness of minor remnants of support material along the bottom face of the specimen. All specimens of each type were similar in terms of gage section dimensions and mass, with outliers being Sample 4 of tensile specimens due to its greater gage width and Sample 1 of the torsion specimens due to its smaller gage diameter. An increased mass was observed for specimens as compared with theoretically expected sample mass, which may be attributed to over extrusion due to the increased flow rate of 130% used in manufacturing these specimens. Sample 4 also exhibited a considerably larger mass compared with the remainder of tensile specimens manufactured, with Sample 1 exhibiting the smallest mass as compared with the remainder of torsion specimens manufactured. This was found to impact the tensile/torsional properties exhibited by these specimens as discussed further on in the results section.

Table 4: MEAM IN718 Tensile & Torsion Test Specimen Dimensions and Mass

	Tensile Specimens			**Torsion Specimens**	
Sample #	**Average Gage Width (mm)**	**Average Gage Thickness (mm)**	**Average Mass (g)**	**Average Gage Diameter (mm)**	**Average Mass (g)**
Theoretical	13.00	3.20	27.9100	5.33	19.8200
1	13.30	3.12	30.1850	5.37	18.8067
2	13.31	3.13	30.1861	5.90	24.3869
3	13.18	3.13	30.2065	5.85	24.3255
4	13.62	3.13	35.9164	5.83	24.2012
5	13.23	3.15	30.1041	5.81	24.2238
6	13.24	3.16	30.4633	5.78	24.2615
7	13.30	3.16	30.4292	-	-
Average ± Standard Deviation	13.31 ± 0.133	3.14 ± 0.015	31.070 ± 1.982	5.76 ± 0.18	23.3676 ± 2.041

The stress-strain response for each of the six samples tested under monotonic tension and torsional loading are shown in Fig 6a and Fig 6b, respectively. The resulting tensile and torsional mechanical properties (i.e., tensile strength, shear strength, elastic modulus, shear modulus etc.) determined are presented in Table 5.

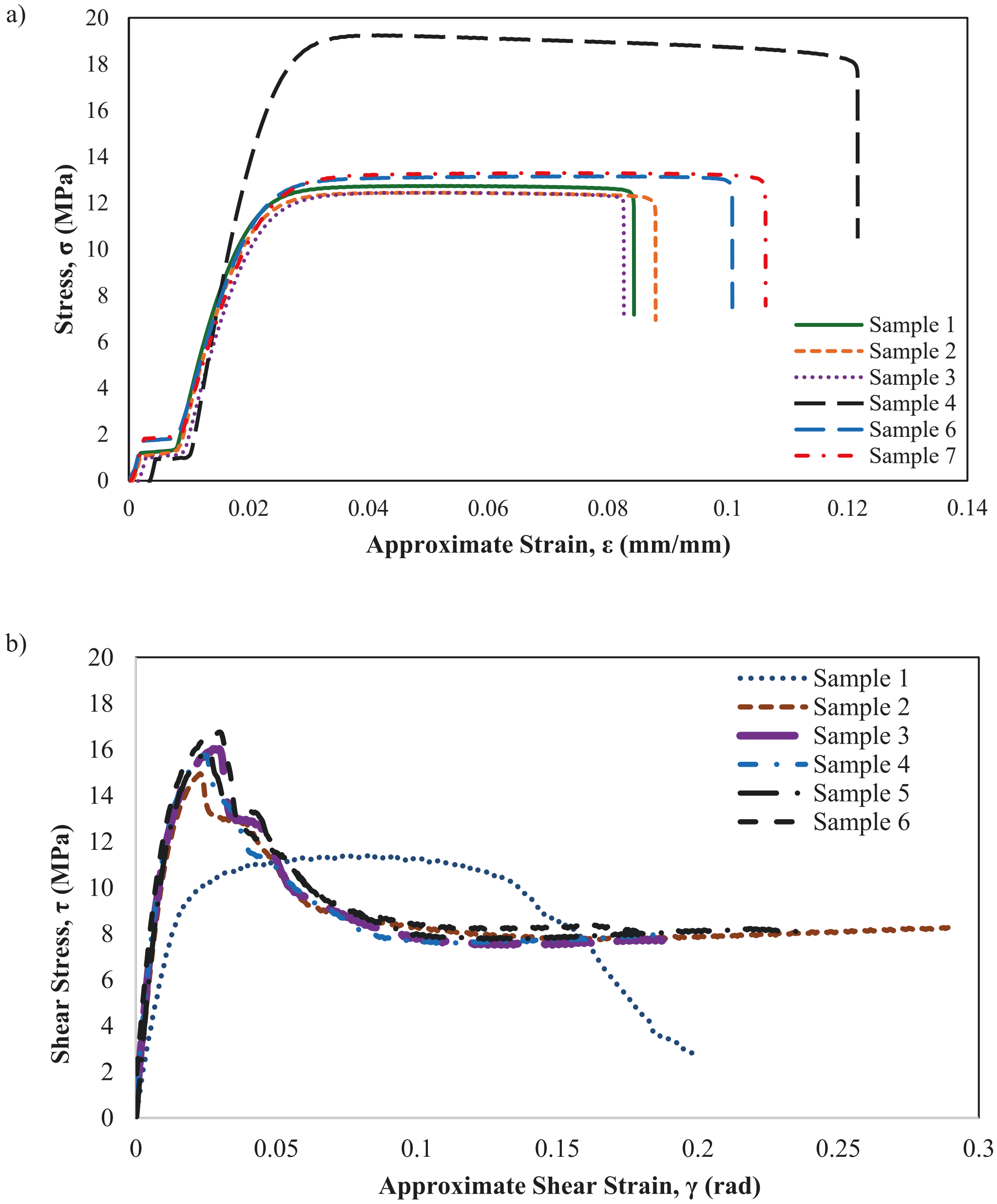

Fig. 6: Mechanical performance of as-built (green state) MEAM IN718: a) Tensile stress-strain response, b) Shear stress- shear strain response

Table 5: Tensile and Torsional mechanical properties of MEAM IN718 in as-Built (green state) samples

	Tensile Specimens			Torsion Specimens			
Sample #	**Tensile Strength, σ_{uts} (MPa)**	**Approximate Elastic Modulus, E (MPa)**	**Approximate Elongation(%)**	**Maximum Torque, T_{max} (N-m)**	**Approximate Max Angle of Twist, φ_{max} (deg)**	**Shear Strength, τ (MPa)**	**Approximate Shear Modulus, G (MPa)**
1	12.738	1038.6	8.434	0.34679	214.08	11.405	753.14
2	12.448	1019.1	8.795	0.60272	280.91	14.946	1203.5
3	12.445	989.18	8.265	0.62993	190.69	16.025	1311.7
4	19.247	1462.6	12.168	0.61266	181.03	15.746	1346.2
5	-	-	-	0.61427	235.41	15.951	1389.4
6	13.153	868.57	10.075	0.63520	181.32	16.753	1368
7	13.293	830.08	10.631	-	-	-	-
Average ± Standard Deviation	13.887 ± 2.419	1034.688 ± 206.114	9.728% ± 1.389%	0.57360 ± 0.1020	213.91 ± 35.67	15.138 ± 1.751	1228.66 ± 220.88

Comparison of tensile properties indicates that Sample 4 exhibited enhanced mechanical performance, as compared with Sample 3 which exhibited the lowest mechanical performance. This is further supported by analyzing the fracture response of Sample 4 (Fig. 7b), which exhibited a much denser internal structure as compared with Sample 3 (Fig. 7a). The presence of considerable interlayer voids across the fracture surface is clearly evident in Fig. 7a as compared with Fig. 7b, which appears to have localized interlayer voids near the specimen edges. Overall, analyzing the failure response of the fractured tensile samples, all six samples were found to exhibit a brittle fracture response. Nevertheless, despite the denser internal structure apparent for Sample 4, presence of MEAM-induced interlayer void is evident through SEM imaging in Fig 7c.

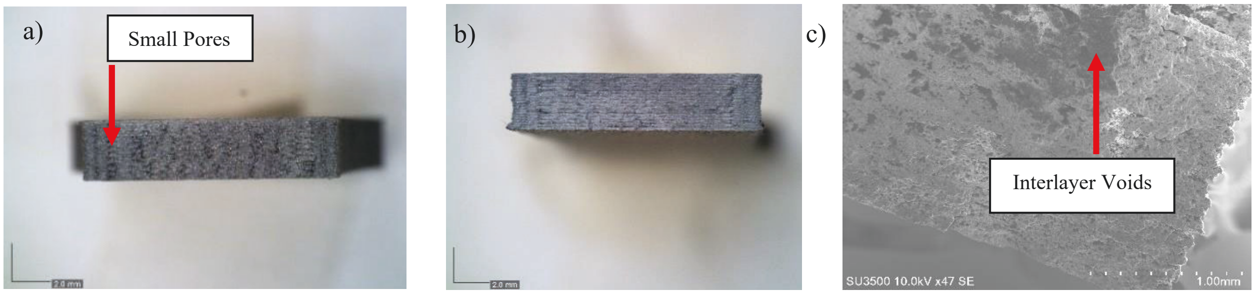

Fig. 7: Brittle fracture response observed for a) Sample 3, showcasing a more porous internal structure and b) Sample 4, showcasing an overall more dense internal structure, and c) SEM imaging of porosity present within Sample 4

Analyzing the failure response of the torsion specimens, all six samples exhibited considerable plastic deformation prior to specimen failure. As highlighted in the experimental section, specimen failure subject to monotonic torsion testing was identified by either complete fracture or significant drop in torque-carrying capacity. Only Sample 1 exhibited a complete fracture. The fracture region of Sample 1, as evident in Figure 8, exhibits torsional cracks both across and between specimen print layers, with failure occurring near radial section of the sample. This sample also had the most significant difference in shear stress-shear strain behavior observed as compared with the remainder of torsion specimens, with a significantly lower maximum applied torque and shear modulus achieved as compared to the other samples. Samples 2-6 exhibited similar monotonic torsional properties, and were considered to have failed after torque readings dropped to approximately 50% of maximum torque achieved with no further signs of decline. As such, the reported maximum angle of twists and shear strain at failure achieved herein are approximate values. Samples 2-6 experienced plastic deformation along the gage section presenting as visibly twisted layers, which appeared to be consistent across all five samples.

Fig. 8: Torsional fracture response of Sample 1

IV. Conclusions and Future Work

This study is novel in that it is the first study to present an analysis of the effects of specimen design and processing parameters on the presence of microstructural defects within as-built (green state) MEAM IN718. Research findings suggest that enhancement to flow rate may result in an increase in part density and lessen the presence of internal porosity for certain specimen geometries. The mechanical response and properties exhibited by these specimens subject to tensile and torsional testing were reported with relatively equivalent performance exhibited across printed specimens, with exceptions of a single outlier in both sample sets. The presence of warping and shrinkage in as-built (green state) MEAM IN718 were observed to be minimal, with an increase in geometric dimensions observed across most specimen designs. Future work will include examining the fatigue performance of as-built MEAM IN718 through further optimization of processing parameters to minimize layer line failures, followed by assessing the impact of the debinding and sintering stages in the manufacturing of fatigue specimens.

Acknowledgments

This material is based upon work supported by the National Science Foundation (NSF) CAREER Grant No. (2338178), awarded to Dr. Sanna F. Siddiqui. The authors would like to acknowledge Dr. Ali P. Gordon, Professor of Mechanical Engineering at the University of Central Florida for use of the MTS Bionix Torsion Test Frame in conducting a select set of experiments for this study. The authors would like to acknowledge Mr. Dustin Fandetti for his assistance with printing select specimens.

References

[1] Qi, H., Azer, M., and Ritter, A., "Studies of Standard Heat Treatment Effects on Microstructure and Mechanical Properties of Laser Net Shape Manufactured INCONEL 718," *Metallurgical and Materials Transactions A*, Vol. 40A, No. 10, 2009, pp. 2410–2422. https://doi.org/10.1007/s11661-009-9949-3

[2] Hosseini, E., and Popovich, V.A., "A Review of Mechanical Properties of Additively Manufactured Inconel 718," *Additive Manufacturing*, Vol. 30, 2019, p. 100877. https://doi.org/10.1016/j.addma.2019.100877

[3] Vafadar, A., Guzzomi, F., Rassau, A., and Hayward, K., "Advances in Metal Additive Manufacturing: A Review of Common Processes, Industrial Applications, and Current Challenges," *Applied Sciences*, Vol. 11, No. 3, 2021, p. 1213. https://doi.org/10.3390/app11031213

[4] Do, T., Kwon, P., and Shin, C.S., "Process Development toward Full-Density Stainless Steel Parts with Binder Jetting Printing," *International Journal of Machine Tools & Manufacture*, Vol. 121, 2017, pp. 50–60. https://doi.org/10.1016/j.ijmachtools.2017.04.006

[5] Babuska, T.F., Krick, B.A., Susan, D.F., and Kustas, A.B., "Comparison of Powder Bed Fusion and Directed Energy Deposition for Tailoring Mechanical Properties of Traditionally Brittle Alloys," *Manufacturing Letters*, Vol. 28, 2021, pp. 30–34. https://doi.org/10.1016/j.mfglet.2021.02.003

[6] Ansari, M., Jabari, E., and Toyserkani, E., "Opportunities and Challenges in Additive Manufacturing of Functionally Graded Metallic Materials via Powder-Fed Laser Directed Energy Deposition: A Review," *Journal of Materials Processing Technology*, Vol. 294, 2021, p. 117117. https://doi.org/10.1016/j.jmatprotec.2021.117117

[7] Siddiqui, S.F., Fasoro, A.A., and Gordon, A.P., "Selective Laser Melting (SLM) of Ni-Based Superalloys," *Additive Manufacturing Handbook*, edited by Badiru, A.B., Valencia, V.V, and Liu, D., CRC Press, 2017.

[8] Siddiqui, S.F., and Araiza, E., "Microstructural Defects Governing Torsional Fatigue Failure of Additively Manufactured As-Built and Heat-Treated Inconel 718," *Engineering Failure Analysis*, Vol. 144, 2023, p. 106975. https://doi.org/10.1016/j.engfailanal.2022.106975

[9] DebRoy, T., Wei, H. L., Zuback, J.S., Mukherjee, T., Elmer, J.W., Milewski, J.O., Beese, A.M., Wilson-Heid, A., De, A., and Zhang, W., "Additive Manufacturing of Metallic Components – Process, Structure and Properties," *Progress in Materials Science*, Vol. 92, 2018, pp. 112–224. https://doi.org/10.1016/j.pmatsci.2017.10.001

[10] Pandey, A., and Gaur, V., "Study on Fatigue Damage in Additively Manufactured IN718 Alloy," *Procedia Structural Integrity*, Vol. 42, 2022, pp. 1017–1024. https://doi.org/10.1016/j.prostr.2022.12.128

[11] Mostafaei, A., Zhao, C., He, Y., Reza Ghiaasiaan, S., Shi, B., Shao, S., Shamsaei, N., Wu, Z., Kouraytem, N., Sun, T., Pauza, J., Gordon, J. V., Webler, B., Parab, N. D., Asherloo, M., Guo, Q., Chen, L., and Rollett, A. D., "Defects and Anomalies in Powder Bed Fusion Metal Additive Manufacturing," *Current Opinion in Solid State and Materials Science*, Vol. 26, No. 2, 2022, p. 100974. https://doi.org/10.1016/j.cossms.2021.100974

[12] Gaytan, S.M., Murr, L.E., Medina, F., Martinez, E., Lopez, M.I., and Wicker, R.B., "Advanced Metal Powder Based Manufacturing of Complex Components by Electron Beam Melting," *Materials Technology*, Vol. 24, No. 3, 2009, pp. 180–190. https://doi.org/10.1179/106678509X12475882446133

[13] Lotfizarei, Z., Mostafapour, A., Barari, A., Jalili, A., and Patterson, A.E., "Overview of Debinding Methods for Parts Manufactured Using Powder Material Extrusion," *Additive Manufacturing*, Vol. 61, 2023, p. 103335. https://doi.org/10.1016/j.addma.2022.103335

[14] Ramazani, H., and Kami, A., "Metal FDM, a New Extrusion-Based Additive Manufacturing Technology for Manufacturing of Metallic Parts: A Review," *Progress in Additive Manufacturing*, Vol. 7, No. 4, 2022, pp. 609–626. https://doi.org/10.1007/s40964-021-00250-x

[15] Bankapalli, N. K., Gupta, V., Saxena, P., Bajpai, A., Lahoda, C., and Polte, J., "Filament Fabrication and Subsequent Additive Manufacturing, Debinding, and Sintering for Extrusion-Based Metal Additive Manufacturing and their Applications: A Review," *Composites Part B: Engineering*, Vol. 264, 2023, p. 110915. https://doi.org/10.1016/j.compositesb.2023.110915

[16] Thompson, Y., Zissel, K., Förner, A., Gonzalez-Gutierrez, J., Kukla, C., Neumeier, S., and Felfer, P., "Metal Fused Filament Fabrication of the Nickel-Base Superalloy IN 718," *Journal of Materials Science*, Vol. 57, No. 21, 2022, pp. 9541–9555. https://doi.org/10.1007/s10853-022-06937-y

[17] Ferro, P., Fabrizi, A., Elsayed, H.S.A., Berto, F., and Savio, G., "Creating IN718-High Carbon Steel Bi-Metallic Parts by Fused Deposition Modeling and Sintering," *Procedia Structural Integrity*, Vol. 47, 2023, pp. 535–544. https://doi.org/10.1016/j.prostr.2023.07.071

[18] Di, K., Zhao, H., Huang, Z., Ma, Z., Wu, S., and Li, M., "High Temperature Oxidation Behavior and Oxide Film Properties of IN718 Alloy after Heat Treatment by Hot Pressing Sintering," *Materials Today Communications*, Vol. 37, 2023, p. 107583. https://doi.org/10.1016/j.mtcomm.2023.107583

[19] Zhang, Y., Li, S., Liu, X., Li, X., Duan, W., Li, L., Liu, B., and Wang, G., "Additive Manufacturing and Characterization of Microstructure Evolution of Inconel 718 Superalloy Produced by Vat Photopolymerization," *Additive Manufacturing*, Vol. 61, 2023, p. 103367. https://doi.org/10.1016/j.addma.2022.103367

[20] Gonzalez-Gutierrez, J., Thompson, Y., Handl, D., Cano, S., Schuschnigg, S., Felfer, P., Kukla, C., Holzer, C., and Burkhardt, C., "Powder Content in Powder Extrusion Moulding of Tool Steel: Dimensional Stability, Shrinkage and Hardness," *Materials Letters*, Vol. 283, 2021, p. 128909. https://doi.org/10.1016/j.matlet.2020.128909

[21] Léonard, F., and Tammas-Williams, S., "Metal FFF Sintering Shrinkage Rate Measurements by X-Ray Computed Tomography," *Nondestructive Testing and Evaluation*, Vol. 37, No. 5, 2022, pp. 631–644. https://doi.org/10.1080/10589759.2022.2085702

[22] Chlebus, E., Gruber, K., Kuźnicka, B., Kurzac, J., and Kurzynowski, T., "Effect of Heat Treatment on the Microstructure and Mechanical Properties of Inconel 718 Processed by Selective Laser Melting," *Materials Science and Engineering: A*, Vol. 639, 2015, pp. 647–655. https://doi.org/10.1016/j.msea.2015.05.035

[23] Melzer, D., Džugan, J., Koukolíková, M., Rzepa, S., and Vavřík, J., "Structural Integrity and Mechanical Properties of the Functionally Graded Material Based on 316L/IN718 Processed by DED Technology," *Materials Science and Engineering: A*, Vol. 811, 2021, p. 141038. https://doi.org/10.1016/j.msea.2021.141038

[24] Gribbin, S., Bicknell, J., Jorgensen, L., Tsukrov, I., and Knezevic, M., "Low Cycle Fatigue Behavior of Direct Metal Laser Sintered Inconel Alloy 718," *International Journal of Fatigue*, Vol. 93, 2016, pp. 156–167. https://doi.org/10.1016/j.ijfatigue.2016.08.019

[25] Nezhadfar, P.D., Johnson, A.S., and Shamsaei, N., "Fatigue Behavior and Microstructural Evolution of Additively Manufactured Inconel 718 under Cyclic Loading at Elevated Temperature," *International Journal of Fatigue*, Vol. 136, 2020, p. 105598. https://doi.org/10.1016/j.ijfatigue.2020.105598

[26] Jirandehi, A.P., Hajshirmohammadi, B., Carrion, P., Khonsari, M. M., Shamsaei, N., and Shao, S., "Strain Energy-Based Fatigue Failure Analyses of LB-PBF Inconel 718: Effect of Build Orientation," *Additive Manufacturing*, Vol. 52, 2022, p. 102661. https://doi.org/10.1016/j.addma.2022.102661

[27] Gribbin, S., Ghorbanpour, S., Ferreri, N. C., Bicknell, J., Tsukrov, I., and Knezevic, M., "Role of Grain Structure, Grain Boundaries, Crystallographic Texture, Precipitates, and Porosity on Fatigue Behavior of Inconel 718 at Room and Elevated Temperatures," *Materials Characterization*, Vol. 149, 2019, pp. 184–197. https://doi.org/10.1016/j.matchar.2019.01.028

[28] "Configuration Wizard," Prusa Research, 2024. Retrieved 28 November 2024. https://help.prusa3d.com/article/configuration-wizard_1754

[29] S.F. Siddiqui, D. Fandetti, and O. Scott-Emuakpor, "Mechanical Performance and Material Characterization of Fused Filament Fabricated ABD 900 Superalloy," ASME Turbo Expo Conference Proceedings, 2024, https://doi.org/10.1115/GT2024-121425.

[30] "3D Printing Pure Metal with Filamet^{TM}," The Virtual Foundry, Inc. Retrieved 28 November 2024. https://thevirtualfoundry.com/print/

[31] Spoerk, M., Arbeiter, F., Cajner, H., Sapkota, J., and Holzer, C., "Parametric Optimization of Intra- and Inter-Layer Strengths in Parts Produced by Extrusion-Based Additive Manufacturing of Poly(Lactic Acid)," *Journal of Applied Polymer Science*, Vol. 134, No. 41, 2017. https://doi.org/10.1002/app.45401

[32] Zhao, X., Chen, J., Lin, X., and Huang, W., "Study on Microstructure and Mechanical Properties of Laser Rapid Forming Inconel 718," *Materials Science and Engineering: A*, Vol. 478, Nos. 1–2, 2008, pp. 119–124. https://doi.org/10.1016/j.msea.2007.05.079

[33] "Extrusion multiplier calibration" Prusa Research, 2024. Retrieved 1 December 2024. https://help.prusa3d.com/article/extrusion-multiplier-calibration_2257